View Article Online
DOI: 10.1039/C8NR07453D

Received 00th January 20xx,
Accepted 00th January 20xx

DOI: 10.1039/x0xx00000x

www.rsc.org/

Nanoclusters of crystallographically aligned nanoparticles for magnetic thermotherapy: aqueous ferrofluid, agarose phantom and *ex vivo* melanoma tumour assessment.

D. Coral[a,b], P. A. Soto[c], V. Blank[c], A. Veiga[d], E. Spinelli[d], S. Gonzalez[d], G.P. Saracco[e], M.A. Bab[e], D. Muraca[f], P.C.Setton-Avruj[c], A. Roig[g], L.Roguin[c], M. B. Fernández van Raap[a,†]

Magnetic hyperthermia is an oncologic therapy where magnetic nanostructures, under a radiofrequency field, act as heat transducers increasing tumour temperature and killing cancerous cells. Nanostructure heating efficiency depends both on the field conditions and on the nanostructure properties and mobility inside the tumour. Such nanostructures are often incorrectly bench-marketed in colloidal state and using field settings far off from the recommended therapeutic values. Here, we prepared nanoclusters composed of iron oxide magnetite nanoparticles crystallographically aligned and their specific absorption rate (SAR) values were calorimetrically determined in physiological fluids, agarose-gel-phantoms and *ex vivo* tumours extracted from mice challenged with B16-F0 melanoma cells. A portable, multipurpose applicator using medical field settings; 100 kHz and 9.3 kA m^{-1}, was developed and the results were fully analysed in terms of nanoclusters structural and magnetic properties. A careful appraisal of the nanoclusters heating capacity in the three milieus clearly indicate that the SAR values of fluid suspensions or agarose-gel-phantoms are not adequate to predict real tissue temperature rise or the dosage needed to heat a tumour. Our results show that besides nanostructure mobility, perfusion and local thermoregulation, nanostructures distribution inside the tumour plays a key role in the effective heating. A suppression of magnetic material effective heating efficiency appears in tumour tissue. In fact, dosage had to be much increased, from the SAR values predicted from fluid or agarose to achieve the desired temperature increase. These results represent an important contribution towards the design of more efficient nanostructures and towards clinical translation of hyperthermia.

[a.] *Instituto de Física de La Plata (IFLP- CONICET), Departamento de Física, Facultad de Ciencias Exactas, Universidad Nacional de La Plata (UNLP), c.c. 67, 1900 La Plata, Argentina.*
[b.] *Institución Universitaria CESMAG, Pasto-Colombia.*
[c.] *Fac. de Farmacia y Bioquímica, UBA, Instituto de Química y Físico Química Biológicas A. Paladini, (IQUIFIB-CONICET), Junín 954 (C1113AAD) CABA.*
[d.] *Instituto de Investigaciones en Electrónica, Control y Procesamiento de Señales (LEICI-CONICET), Departamento de Electrotecnia, Facultad de Ingeniería, Universidad Nacional de La Plata (UNLP).*
[e.] *Instituto de Investigaciones Fisicoquímicas Teóricas y Aplicadas (INIFTA), UNLP, CCT La Plata - CONICET, Casilla de Correo 16 Sucursal 4 (1900) La Plata, Argentina.*
[f.] *Laboratório de Materiais e Dispositivos, Instituto de Física 'Gleb Wataghin', Universidade Estadual de Campinas, Campinas, Brazil.*
[g.] *Institut de Ciència de Materials de Barcelona, ICMAB-CSIC, 08193, Bellaterra, Catalonia, Spain.*

† Corresponding author: raap@fisica.unlp.edu.ar, phone: +54 221 4246062, Fax +54 221 4236335

Electronic Supplementary Information (ESI) available: Procedures for M vs. H curves for fitting and SAR values semi-empirical calculation. Field inductor design discussion. Fig. S1: TEM histograms. Fig. S2-S7: HRTEM NCs images and FFT. Fig. S8: Magnetization curves at 300 K. Fig. S9: heating curves of aqueous nanoclusters suspensions. Fig S10. Cryo-TEM images of B16-F0 cells incubated with NCs. See DOI: 10.1039/x0xx00000x

Introduction

Colloidal dispersions of magnetic nanoparticles (MNPs) in physiological fluids have shown great potential as heat mediators for hyperthermia oncologic therapy[1]. Briefly, magnetic hyperthermia (MH) is the modality among thermotherapies that use MNPs and an alternating magnetic field (AMF) in the radiofrequency range to increase solid tumours temperature. The MNPs absorbs energy from the field to release it to its environment through Néel and Brown relaxation mechanisms[2].

MH relies on two facts: large doses of intratumourally-injected nanoparticles can generate enough heat to inflict damage to cancer cells and that the overall blood flow tends to be significantly lower in certain poorly vascularized tumour areas with respect to well-vascularized normal tissues[3], ensuring tumour selectivity by minimizing heating of adjacent healthy tissue. Tumour cancer cells apoptosis is induced when tissue temperature reaches therapeutic values (43-45 ^{o}C)[4] whilst cell/tumour ablation occurs above 45 ^{o}C. Tissue temperature elevation can also be used to improve cancer cells sensitivity to radiation and/or to anticancer drugs. MH recently received EU-wide regulatory approval as medical devices for the

View Article Online
DOI: 10.1039/C8NR07453D
ARTICLE
Journal Name

treatment of brain tumours. Previous clinical trials of MH combined with radiotherapy[5,6] indicated survival benefit of 7.2 and 8.6 months for first tumour recurrence and primary tumour, respectively. Those results reinforce the idea that improvement in the detailed understanding of this procedure is still needed.

The most widely used nanomaterial in hyperthermia is iron oxide (magnetite and maghemite nanoparticles) due to its low cytotoxicity[7], large biocompatibility and approval by the FDA and EMA. Over the last years, efforts on MNPs-mediated hyperthermia have been directed to reach specific absorption rate (SAR) values close to 1 kW g^{-1}. As SAR increases with increasing field frequency f and amplitude H_0, a very careful attention must be paid to these values. Indeed, a too strong field may generate Eddy currents and cause non-specific heating and therefore damaging healthy tissues and overheating of cancer tissues. In spite of this, many research groups still characterize their newly produced colloids at f and H_0 values highly exceeding the recommended threshold value for major discomfort[8,9], given by $H_0f < 5x10^8$ A m^{-1} s^{-1}, and even over the more conservative value[10] of $H_0f < 50x10^8$ A m^{-1} s^{-1}. Besides Atkinson[9] clinical tolerance test, performed in healthy volunteers, the first clinical application of interstitial hyperthermia, using MNPs in locally recurrent prostate cancer, indicated that pre-treatment planning had to be altered because the patients experienced discomfort when the field strength was increased above 5 kA m^{-1} at a frequency of 100 kHz[11], clinically establishing a particular biologically safe range. Note that treatments in human patients are carried out at specially designed applicator of variable field amplitude lower than 18 kA m^{-1} and fixed frequency of 100 kHz[12].

In addition, MNPs characterization at high fields lead also to the problem that heating potential could later be insufficient for applications under field clinical conditions. Indeed, the higher the SAR, the lower the dosage needed to achieve a therapeutic temperature, which is crucial because too high dosages may induce significant toxicity and clearance issues[13].

The various strategies tested to enhance the heating power, mainly proceed by varying MNPs size, shape, composition and more recently their structuration. Below, we briefly review previous results, we stress the fact that nanostructure optimization has been systematically carried out at field values far away from clinical settings and with MNPs dispersed in liquids, a model very far from a real tumour scenario.

Regarding size, crystalline spherical magnetite nanoparticles with core sizes between 20 and 30 nm, in the transition zone between single magnetic domain and multidomain[14] were proposed as well suited for MH with SAR value about 300 W g^{-1} for 22 nm at 77 kHz and 40 kA m^{-1} i.e. at a field setting corresponding to H_0f value equal to 6.2 times the threshold value (TV) of 5×10^8 A m^{-1} s^{-1}. Cubic shape particles also display large SAR values due to shape anisotropy contribution[15,16]. Guardia et al[15] reported 509 W g^{-1} at 320 kHz and 15 kAm^{-1}(9.6 times the TV) for a 19 nm cubic nanoparticle and Martinez-Boubeta et al[16] reported 150 W g^{-1} at 765 kHz and 12 kA m^{-1}, 18 times the TV, for 20 nm cubic particle. The nanostructuration of single-core magnetite to multi-core structure resulted in a SAR increase from 150 W g^{-1} to 1604 W g^{-1}under field conditions of 29 kA m^{-1} and 520 kHz[17] (30 times the TV). Spherical clusters (60 nm size) of carboxymethyldextran (CMD) coated iron oxide nanoparticles of 18 nm dissipate 720 W g^{-1} when excited at 10 kA m^{-1} and 410 kHz[10] (8.2 times the TV) and nanoflower like assemblies[18] dissipating 1175 W g^{-1} when excited at 21.5 kA $m^{-1}$and 700 kHz (30 times the TV) has also been reported. Another way to improve the SAR is by modifying MNP chemical composition, for instance by doping with Zn, Mn or Co. We have reported SAR value of 367 W g^{-1} at 260 kHz and 41 kA m^{-1} (21 times TV) using a 16 nm size particle with 3.3 % of Fe atoms replaced by Zn[19]. For Co substitution[20], 440 W $g^{-1}$was obtained at 700 kHz and 24.7 kA m^{-1}(35 times TV) and Mn substitution[21]effectively leads to an increase in the MNPs heating efficiency. Interesting, using exchange coupled nanomagnets[22], combining hard and soft magnetic phases like $CoFe_2O_4$@$MnFe_2O_4$, a SAR value two order of magnitude larger was reported for 15 nm composite particle in comparison with the values for its components (9 nm $CoFe_2O_4$ and 15 nm $MnFe_2O_4$) at 500 kHz and 37.3 kA m^{-1}, (37 times the TV). Composition modification comparing with iron oxides entails the problem of increasing cytotoxicity.

Regarding to the effects related to the interaction between MNPs and biological entities, SAR values appear highly suppressed when MNPs are located in cells as described in various *in vitro* assays[20,23–27].The pioneering work of Fortin *et al*[20] related this attenuation to the inhibition of Brown contribution to heat generation, due to abrupt change in media viscosity. Also, significant reductions in cell viability without macroscopic cell cultures temperature rise has been reported for various cancer cells with MNPs internalised and exposed to AMF, like in Hella cells loaded with silica-coated manganese oxide[27] and in dendritic cells loaded with magnetite having either positive (NH+2) or negative (COOH−) surface functional groups[28] as well as in the case of nanoparticles engineered for targeted hyperthermia as CMD coated magnetite conjugated with epidermal growth factor (EGF) in MDA-MB-468 and MCF-7 cells[23,26]. More recently, De Sousa et al[24] provided evidence that there was local heating even though no global temperature increase was sensed. To this end, human lung adenocarcinoma cells (A549 cell line) were transduced with a lentiviral vector encoding the expression of the enhanced green fluorescence protein (EGFP) under the action of the inducible human heat shock protein 70B promoter. These modified cells ($A549^{HSP}$) that express the EGFP under thermal stress. also expressed the EGFP after being loaded with magnetite MNPs and exposed to RF fields indicating that endocyted MNPs create hot spots inside the cells, even though the amount of heat released was not enough to globally increase the cell culture temperature[24]. The need of distinguishing between global heating and cell-treatment efficacy to improved hyperthermia treatment was later discussed elsewhere[25]. Other explanation referred to aggregation inside cell endosomes[29,30]. Jeon *et al*[29] proposed that the formation of super-aggregates in the intracellular milieu impacts on SAR, reducing it from above 200 W g^{-1} for aggregates composed of fewer than 50 primary particles to below 50 W g^{-1} for super-aggregates, and stressed that the underlying physical mechanism by which aggregation leads to reduction in SAR remains unclear. A review on nanoparticle designed for targeted hyperthermia and their interaction with cell of importance in systemic delivery can be found in Kozissnik et al. [31]

On the other hand, the applicability of MH has been proved in animal model[32,33] and in clinical trials[34]; nevertheless the acquisition and analysis of SAR data on *ex vivo* tumour tissue can be barely found. Importantly, the influence of particle immobilization in tumour tissue and their influence in magnetic properties has been addressed by Dutz et al[35]. These authors proved by *ex vivo* analysis of human breast tumours grown in immunodeficient mice injected with multicore

View Article Online
DOI: 10.1039/C8NR07453D

nanoparticles, that a temperature increase owed to Brown relaxation could be neglected due to MNPs rotation suppression. However, they registered a tissue temperature increase of about 20 °C within the first 60 s in a tumour loaded with 7 mg of multicore nanoparticle exposed to an AMF of 400 kHz and 25 kA m^{-1}.

In the present work, we attempt a holistic approach to better comprehend which are the relevant aspects that can facilitate the translation of magnetic hyperthermia to clinical uses. To that, we focus in one of the most promising type of material reported so far[18], in fabricating a portable multipurpose field applicator with therapeutic specifications and in the material and applicator validation in a tumour model. To this end, we synthesize a flower like nanostructures and proved that they satisfied biomedical requirements, we designed and built a field applicator that works with therapeutic specifications and then, we focus on the issue of tumour heating efficiency in a tumour model at field conditions close to therapeutic ones.

Nearly monodisperse citrate coated nanoclusters (NCs) of crystallographically aligned magnetite MNPs were fabricated by a co-precipitation polyol method. A meaningful structural and magnetic characterization was carried out to resolve NCs composing particles collective behaviour and to support SAR data analysis. Tumour *ex vivo* analysis was selected to study static tissue properties. Melanoma tumours grown in C57BL/6J mice challenged with murine B16-F0 melanoma cells were extracted after mice sacrifice and selected as the *ex vivo* tumour model. The applicability and dose-response characteristic of selected NCs were *ex vivo* tested and compared with the SAR values of these NCs dispersed in water and agarose-gel-phantoms.

Results and discussion

A. Nanocluster suspensions synthesis and properties.

Among the various types of nanostructures reported for MH, nanoclusters composed of primary MNPs crystallographically aligned with adjacent ones are the most promising candidates to improve magnetic heating. The first method for achieving such nanocluster was presented by Ge et al[36],who reported a protocol for the preparation of polyacrylate-capped superparamagnetic magnetite (Fe_3O_4) clusters with tuneable sizes from 30 to 180 nm by one step high-temperature hydrolysis process. These NCs exhibited good stability and high dispersibility in aqueous media (water), without any further functionalization. Since the biodegradability and biocompatibility of the polyacrylic acid attached on the magnetic clusters is unclear[37,38], we choose to modify a synthetic variation recently proposed by Hougouneng et al[18], of citrate coated NCs. The formation and growth rate of iron oxide nanoparticles in the presence of this polyol mixture is slow and the nanoparticles have enough time to rotate and contact with neighbour nanoparticles at the angle minimizing energy. Some misalignment between particles disappear during Ostwald ripening process[39].

Nanocluster size and component particle size distributions, their crystalline structure and the degree of alignment inside the nanocluster NCs were characterized by means of Transmission Electron Microscopy and Electron Diffraction. Representative HR-TEM images of the NCs are shown in Figure 1. The images corroborate that the polyol procedure, using DEG/NMDEA 1:1 (v/v), yields nearly monodisperse multi-core nanostructures. No isolated particles were observed. Size histograms were constructed by measuring and counting NCs and composing MNPs sizes from several micrographics of each sample. Histograms are shown in Figure S1 of ESI file. The so derived mean nanocluster diameter D_{NC} and nanoparticle D_{NP} diameter and their standard deviation (s.d) are summarised in Table 1 together with main synthesis parameters. These NCs displays mean sizes between 20 and 35 nm. Hydrodynamic sizes (D_{HYD}) of NC in aqueous suspensions range between 22 and 45 nm as seen in Table 1. For sample NC20 suspended in a 1% PBS solution D_{HYD} is 29±7 nm.

Table 1. NC synthesis conditions and structural properties. T_i is the initial temperature, t_s is the time during which the solution was kept at 220 °C, D_{NC} and D_{NP} are nanocluster and primary particle diameters determined from HR-TEM, D_{HYD} is the hydrodynamic size, of the NC dispersed in water, deduced from Dynamical Light Scattering (DLS) number distribution.

SAMPLE	T_i *(°C)*	t_s *(h)*	D_{NC} ± *s.d* (nm)	D_{NP} ± *s.d* (nm)	D_{HYD} (nm)
NC20	15	12	20±7	9±3	22±7
NC26	17	13	26±6	8±3	29±10
NC34	30	13	34±4	8±2	45±14

Selected area electron diffraction (SAED) pattern shown at the inset of Figure 1d was indexed with a cubic spinel structure (space group Fd3m, card #750449). When selected area includes many NCs the image displays diffraction rings in agreement with different directions contributions of the randomly oriented NCs. When just one cluster is selected as shown in the left inset of Figure 2c, diffraction spots appear in agreement with Fourier transformation (FT at the centre of a NC with the edge of several nanoparticles) of marked areas confirming the crystallographic alignment of the MNPs forming a NC. The continuity of the crystal lattice planes across nanoparticles boundaries can be clearly observed in Figure 1b (additional TEM images are presented in Figures S2 to S7 of ESI file). In addition, the filtered FT of a NC from NC20, shown in Figure 2a, reveals that this NC is composed of primary particles exposing interplanar distance 0.26±0.03 nm corresponding to the (311) plane but along two orientations forming an angle of 33°, see Figure2b.

These nanostructures to be ideal materials for biomedical application must conjugate large magnetic susceptibility with sizes within magnetic single domain range assuring superparamagnetic behaviour and consequently null magnetization at zero applied field, stability in biomedical fluids and low toxicity.

View Article Online
DOI: 10.1039/C8NR07453D
ARTICLE
Journal Name

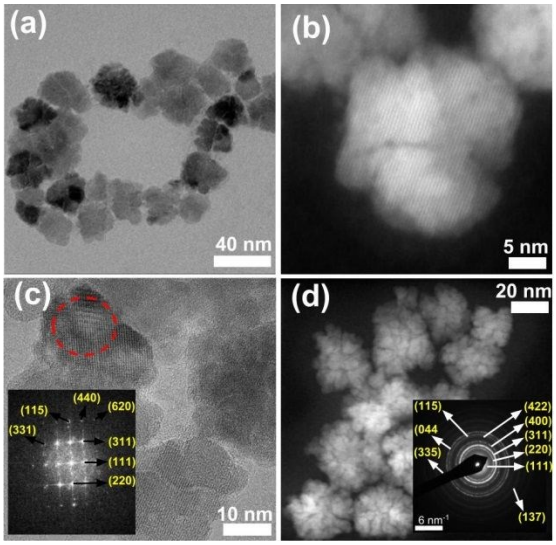

Figure 1: HR-TEM and STEM of NC26 panels (a), (b) and (c) and of NC34 (d). Insets in: (c) Fourier transformation of the areas inside the red circles, and (d) is the electron diffraction pattern including many NCs displaying rings in agreement with their random orientation. Indexed with the spinel structure.

The MNPs composing the NCs display mean sizes (D_{NP}) of about 8 nm, being clearly within single magnetic domain range. On the other hand, each NC of volume V_{NC} is a collection of single domain particles of magnetic volume V_{NP} and giant magnetic moment $\mu_{NP} = M_s.\rho.V_{NP}$ (ρ is the mass density for magnetite, 5175 kg m^{-3}). HR-TEM data shows crystallographic alignment between MNPs, but how their magnetic moments are arranged is still not clear and we further investigated here. In a recent report, we proved[40] that the data needed to predict the SAR of a magnetic colloid are the saturation magnetization M_s, mean nanoparticle volume V_{MNP} and a mean activation energy <*U*>. Where <*U*> includes, besides the anisotropy term equal to KV_{MNP} (where *K* is the magnetic anisotropy constant) contributions due to size and shape polydispersity, aggregation and dipolar interactions among particles. In general, an increase in polydispersity and/or aggregation tends to lower the SAR, while an increase in magnetic interactions strength results in a SAR increase. A rational choice of independent experiments allowed us to derive consistent <*U*> values that were successfully used to reproduce the SAR of various nanoparticle suspensions[40]. Following a similar methodology, in this work we first measured the isothermal magnetization field dependence at 300 K of the NCs in aqueous suspensions, exemplified in Figure 3a for the NC20 (see fitting details in section S1 in the ESI file). The *M vs. H* loop displays no coercive field in agreement with unblocked NCs performing Brownian motion.

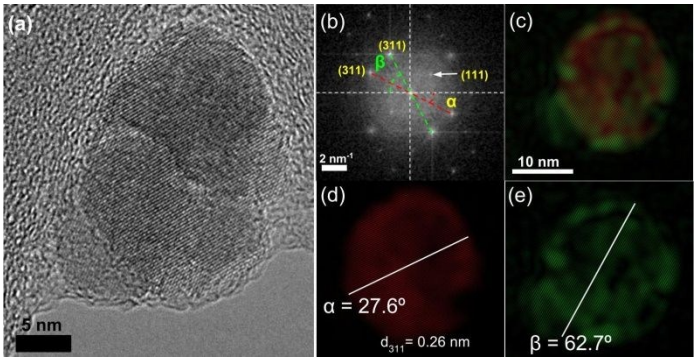

Figure 2: (a) HR-TEM of one nanocluster from NC20 and its Fourier transform (b) indexation is consistent with electron beam parallel to the $[01\bar{1}]$ direction of magnetite. (c) Filtered Fourier transform showing two orientations of the same crystallographic plane, green and red colours correspond to the (311) planes forming an angle of 61° and 28° with horizontal axis.

The M_s and mean magnetic moment μ_M were derived from the fitting of *M vs. H* curves with an Langevin type integral that continuously adds contribution from NCs of total magnetic moment distributed following a log-normal distribution, to the magnetization at each field[41]. Fitted parameter are number of nanoclusters *N*/Fe mass, σ_μ standard deviation of $ln(\mu/\mu_0)$, median magnetic moment μ_0, and high field susceptibility χ included by adding a linear term χH. From fitted values saturation magnetization $M_s=N\mu_M$ and the mean moment $\mu_M = \mu_0 \exp(\sigma_\mu^2/2)$ were derived and are listed in Table 2 (Magnetization curves of all the samples, at 300 K, are shown in Figure S8 of the ESI file). The so derived saturation magnetization values are close to bulk magnetite value[42] of 120A m^2 kg$_{Fe}^{-1}$. Only NC34 displays a low M_s value, probably those nanoparticles bears a large magnetic dead layer. Large M_s is one of the requirements to achieve larger SAR values[43] as the SAR depends with the M_s square[2]. These μ_M values are in agreement with NCs size derived from TEM, being much larger than, for instance, the magnetic moment of a single 8 nm spherical particle whose bulk magnetic moment is 10867 μ_B. The latter was estimated using that magnetite magnetic moment is 24 μ_B per unit cell and a lattice constant *a*=8.3963 Å. This analysis indicates that the NCs behave as a single magnetic domain particle shading light in a pending question of the field. If the crystallographic alignment is complete the NCs have cubic magnetic anisotropy with easy axes along [111] direction. This direction form an angle of 22°with the vector (1,3,3) normal to the planes (311) seen in Figure 2. However, for partial alignment, as for example for the NC shown in Figure 2, where a fraction of the composing MNPs has the easy directions at 76.7° relative to the vector (1,3,3) normal to the planes (311) and drawn in red, and the complementary fraction an easy axis forming an angle of 33° with the ease axis of the red part and also at 76.7° relative to the rotated plane normal vector (green). This misalignment could lower NC total magnetic moment as compared to NC with full alignment but is still expected to be larger than that of NCs of randomly oriented MNPs for which SAR decrease[41].

View Article Online
DOI: 10.1039/C8NR07453D

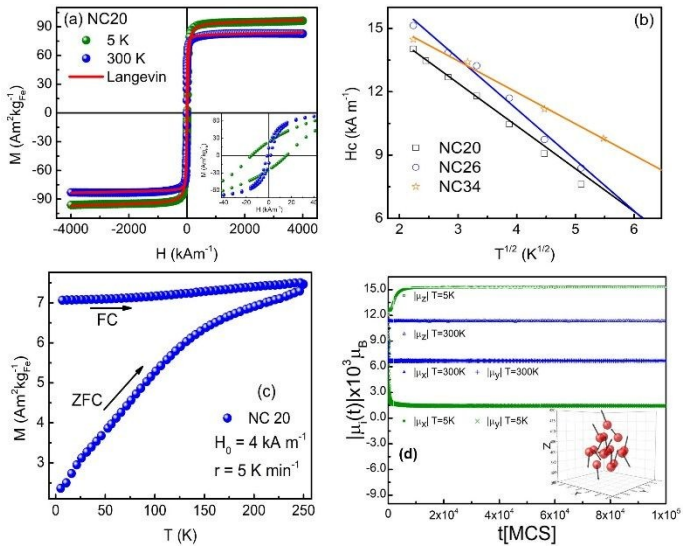

Figure 3: (a) Magnetization loops measured at 5 and 300 K for NC20. *Inset:* zoom showing low field magnetization. Solid lines are for best Langevin fits, (b) Coercive field H_c temperature dependence derived from d.c. magnetization curves. (c) Magnetization under ZFC/FC protocols using DC applied field of 4 kA m^{-1} for NC20. (d) Absolute values of the cluster magnetic moments $|\mu_i|$ as function of the Monte Carlo steps time (MCS) at 5 and 300 K, being $i = x,y,z$ and z coincident with anisotropy axis. Inset in d shows a typical equilibrium configuration of particle magnetic moments at $t = 10^5$ MCS. The particles are shrinked to allow better visualization of the arrows representing the NPs magnetic moments at 300 K.

Then, we measured the hysteresis loop at 5K, shown in Figure 3a for NC20 and H_c values at selected temperatures (6, 8, 15, 20, 26 K) shown in Figure 3b for all the samples. The former was used to estimate an anisotropy field, $H_K = 2K/\mu_0 Ms$, of about 120 kA m^{-1} for our samples. This is an important piece of information since for magnetic hyperthermia experiments increasing the field strength amplitude H_0 to values larger than H_K results in no further SAR improvement. The H_c *vs.* T behaviour was used to semi-empirically derived <U> (using equation 4 in the ESI file) and to calculate SAR using Stoner–Wohlfarth theory[44] as explained elsewhere[40]. Values of <U> and calculated SAR (SAR_c) are listed in Table 2 (for calculation details see S2 section of ESI file). The SAR_c values are in good agreement with those calorimetrically determined at 100 kHz and 9.3 kA m^{-1}, also listed in Table 2 and the heating curves are shown at Figure S9 of ESI file. Importantly, we have shown that SAR of a NCs suspension can be well reproduced using a procedure valid for suspension of single domain MNPs. The FC data acquired using a DC field of 4 kA m^{-1} is exemplified in Figure 3c for NC20. The FC curve do not display any of the characteristics of an antiferromagnetic order[45]. Moreover, to get a better insight on how magnetic moments are arranged in the NCs, we performed a Monte Carlo simulation. Figure 3d shows time dependence of NC magnetization in the easy direction (z-axis) and in the perpendicular directions (x, y) at 5 K and 300 K for a NC composed by 14 single magnetic domain nanoparticle of 8 nm size. The magnetic moment projection on the anisotropy axis (z- direction) is much larger than in the perpendicular directions, i.e. magnetic moments predominantly align in the NC easy direction. A snapshot for 300 K simulation is shown in the inset. The difference between μ_z and $\mu_{x,y}$ becomes larger as temperature is reduced as expected for a ferromagnetic alignment.

As mentioned, to achieve stability the NCs were citrate coated. Z potential results, obtained from Laser Doppler Electrophoresis measurements, indicated ζ values were between -30 and -44 mV confirming that the coating was successful and the nanoclusters are negatively charged. Cytotoxicity was analysed by means of MTT (3-[4,5-dimethylthiazol-2-yl]-2,5 diphenyl tetrazolium bromide) assay, based on the conversion of MTT into formazan crystals by living cells, which determines mitochondrial activity[46]. Results, shown in Figure 4a, indicate that 17 h exposure of B16-F0 cells to 116 μg_{Fe} mL^{-1} of citrate-coated Fe_3O_4 nanoclusters did not significantly affect cell viability.

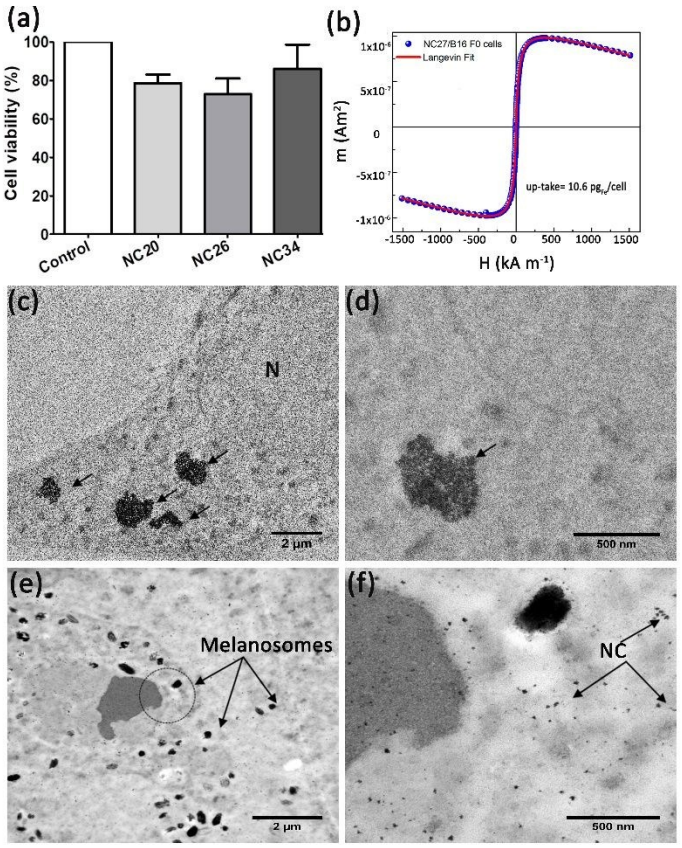

Figure 4: (a) Cell viability derived from MTT assay, (b) and(c) show VSM loop of a pellet of B16-F0 cell culture incubated in medium doped with NCs at a concentration of 116 μg_{Fe} mL^{-1} for 17 h and cryo-TEM of B16-F0 cell incubated with NCs respectively(d) detail of NCs organization inside the cell endosome, (e) TEM of B16-F0 cell in the tumour *in vivo* 24 h after NC20 injection and AMF application.(f) Detail of NCs organization in the cytosol.

From the analysis a magnetic loop (VSM data) of the cell culture after incubation at a concentration of 116 μg_{Fe} mL^{-1} shown in Figure 4b, an

View Article Online
DOI: 10.1039/C8NR07453D
ARTICLE
Journal Name

uptake of about 10.6 pg_{Fe}/cell was obtained. VSM data analysis used to obtained the uptake is described in Experimental section F. The uptake is the result of the NC internalization into endosomes exemplify in Figures 4c and 4d with TEM image (see additional B16-F0 cells TEM images in Figure S10 in the ESI file). Our in vitro results indicate that NC are not cytotoxic for B16-F0 cells and agree with those previously reported for single MNPs[43,47].

Figures 4e and 4f show the NC in the tumour 24 h after *in vivo* NC injection and AMF application as described in section C. The NC distribution in cells of tumour tissue greatly differs from that shown for *in vitro* cell culture. Endosomes densely loaded with NCs and/or the presence of super-aggregates of NCs are absent.

Table 2. Nanocluster aqueous suspensions properties: *[x]* is the Fe mass concentration, μ_M is the NC mean magnetic moment determined from the magnetization curve with saturation magnetization M_s at 300 K. *<U>* is the mean activation energy determined from *Hc vs T* data analysis and *SAR* is the specific absorption rate measured at 100 kHz and 9.3 kA m^{-1}. SAR_c is the specific absorption rate semi-empirically calculated as explained in the text.

SAMPLE	*[x]* ($mg_{Fe}mL^{-1}$)	μ_M ($10^3\mu_B$)	Ms_{300K} ($Am^2 kg^{-1}_{Fe}$)	Ms_{5K} ($Am^2 kg^{-1}_{Fe}$)	H_{K5K} ($kA\ m^{-1}$)	*<U>* (10^{-20} *J*)	*SAR* ($W\ g^{-1}_{Fe}$)	SAR_c ($W\ g^{-1}_{Fe}$)
NC20	7.7±0.1	67±2	79±2	95±1	121	2.8±0.1	5.4±0.2	7.2
NC26	10.4±0.2	70±2	54±2	76±2	159	2.3±0.1	12.2±0.6	9.8
NC34	3.6±0.1	33±1	39±1	48±1	126	6.2±0.3	11.5±0.6	10.3

B. Specific absorption rate measurements.

Once proved that the NCs fulfilled biomedical requirements we analysed their heating efficiency in melanoma tumour tissues, where the NCs unavoidable distribute heterogeneously after injection and compare with the heating efficiency in homogenous NCs dispersions achieved in agarose gel and liquid. As we already noted in the introduction it is extremely important to carry out these analysis at field frequency and amplitude within biomedical safe range. With the aim of using the same device (without modifications) for phantoms, *in vitro* and *in vivo,* we designed and built a portable applicator that can hold large samples and works at 100 kHz and field amplitudes that can be continuously varied between 2 and 15 kA m^{-1} without water-cooling, i.e. at the same frequency and field amplitude range used for clinical trials[12]. Applicators previously designed for MH either are bulky or only useful for small samples. Some use a resonant network with a coil made of hollow-copper-pipe refrigerated with water[48–51] or use Litz wire with ferromagnetic core achieving the desired uniform field in a reduced volume[52–54] not useful for *in vivo* experimentation or for large samples. None of them end up with our portable design (shown in figure 5) that uses parallel LLC resonant network with Litz wire coil and forced air convection cooling and can be transported without requiring specialized installation[55]. Front and side views of the field applicator are shown in Figure 5, where the main components are referenced. Field was continuously sensed during field applications using single turn sensing coil and calibration was achieved with a secondary coil. A full description is placed at the ESI file.

A major challenge when dealing with large samples concerns to field uniformity. In Figure 6 we show a field amplitude simulation over the whole receptacle volume. Due to coil finite length, field variations across the central area relative to the coil centre, where the tumour is placed for field applications, for ±7.5 mm in radial direction results in +1.89% field variation while in the coil exe direction, variations of ±7.5 mm results in -1.45% field variation. For measurements the samples are carefully placed in the centre of the coil and the whole tumour volume (15 mm in diameter) is uniformly affected by the field.

View Article Online
DOI: 10.1039/C8NR07453D

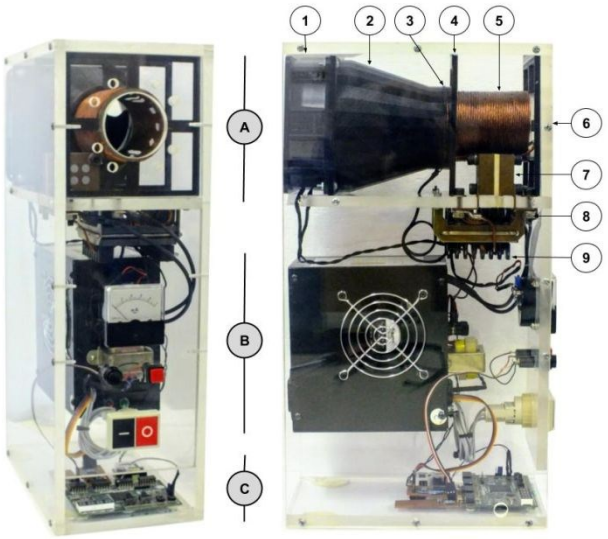

Figure 5: Front and side view of mechanical and electronic parts of the portable AMF field applicator. Main sections: A) high voltage section, B) AC/AC converter (rectifier and inverter), control panel and indicators C) CPLD based digital modulator for frequency and amplitude control. Resonant circuit and cooling: 1) 5" AC fan, 2) air nozzle, 3) single turn sensing coil, 4) plastic mounting brackets, 5) resonant inductor, 6) receptacle, 7) resonant capacitor, 8) copper bars and 9) serial inductor.

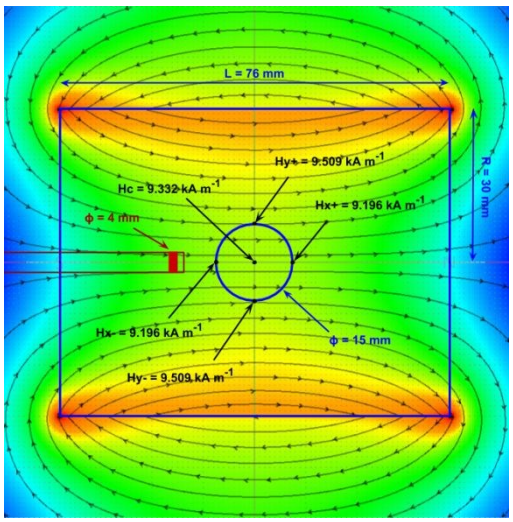

Figure 6: Field amplitude simulation for a Litz wire coil of 30 mm radius and 76 mm length. The circle in the centre stands to represent a 15 mm tumour. In red colour support holding a secondary coil used to calibrate the device.

Time-dependent temperature curves of NCs aqueous suspensions, agarose gel dispersion and *ex vivo* tumours were determined by calorimetric measurements at 100 kHz and 9.3 kA m^{-1} using the portable applicator described. The SAR values of the magnetite nanoclusters aqueous dispersion are listed in Table 2 (see the heating curves in Figure S9 in the ESI file). Notice that for similar size NC of maghemite a value of 1175 $W \cdot g^{-1}$ was reported[18] at 21.5 $kA \cdot m^{-1}$ and 700 kHz. Scaling that SAR value to our field condition, it results in ~36 $W\ g^{-1}$ i.e. in the same order of magnitude of our NCs.

Next, agarose gels phantoms were prepared by adding 1% (m/V) of agarose to 700 µL aqueous suspension after concentration, to immobilize the NCs in the milieu, approaching tumour viscosity and inhibiting Brown contribution to heat generation. The so-prepared samples consist of NCs uniformly distributed in the agarose gel. The measured heating curves are shown in Figure 7a. Based on these results, NC20 and NC34 were selected for the *ex vivo* hyperthermia experiments. The amount of NCs to inject into the tumours, expressed as the mass of Fe (m_{Fe}), was estimated from agarose gel temperature increase.

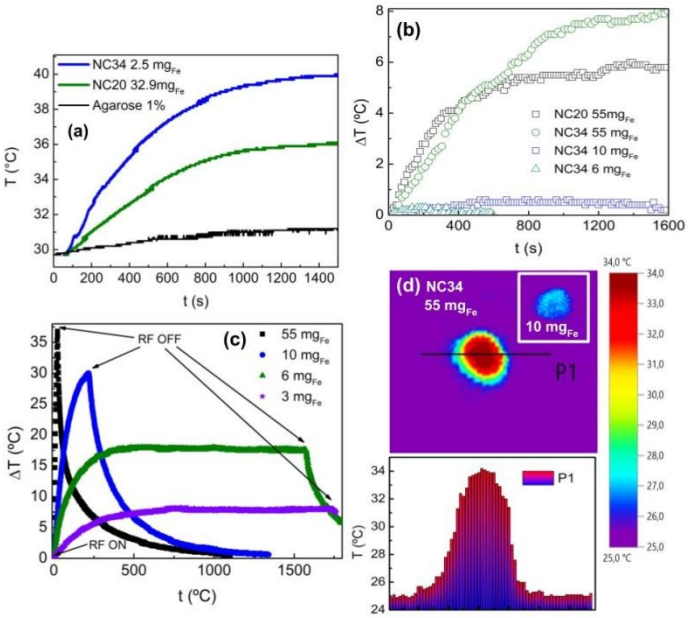

Figure 7: Heating curves of NCs measured in the portable applicator at 100 kHz and 9.3 kA m^{-1} in a) homogenously dispersed in 700 µl of agarose-gel-phantoms and b) in tumour tissue, displayed as temperature increase relative to control. c) Heating curve of NC34 in tumour tissue at 265 kHz and 40 kA m^{-1}. d) Thermal image of heated tumour after recording the heating curve shown in b). Inset in d: thermal image of a tumour injected with 10 mg_{Fe} of NC34, no heating was observed after RF application with optical fiber (panel b) nor with thermal image.

To evaluate NC20 heating efficiency in tumour tissue, experiments were performed with 7 mice. 4 mice received two intratumoural injections, two hour spaced, of 100 µL of NC20 in PBS (a total of 55 mg of Fe), whereas tumours from 3 mice received PBS (control group). After 24 h the mice were sacrificed and tumours were exposed to the AMF. A temperature increase of 7.4± 1.4 ºC was accomplished within

View Article Online
DOI: 10.1039/C8NR07453D
ARTICLE
Journal Name

the first 23 min in NC20 treated-mice (see Table 3 and Figure7b). No significant temperature increasing (ΔT) was observed in control group.
Experiments with NC34 were performed in 12 mice (8 injected with NC34 suspended in PBS and 4 controls only with PBS).Initially, two mice were injected with 3.0 mg_{Fe} of NC34 i.e. the amount of Fe that had produced a ΔT of about 10 ^oC in 700 µL of agarose gel (see Figure 7a). Surprisingly, no temperature increase was achieved in these tumours (see Figure 7b). Notice also that tumour volumes were smaller than the gel volume. Then, a third one received 6 mg_{Fe} and four other mice received 10 mg_{Fe} (see Table 3). Extracted tumours were exposed to the AMF and again no ΔT increase was achieved.
Then, to control the magnetic material, a suspension of NC34 in PBS at a concentration of 50 mg_{Fe} mL^{-1} was exposed to the AMF as well as a dilution 1/12 (4.2 mg_{Fe} mL^{-1}) resulting in ΔT of 8 ^oC and 6.5^oC respectively (not shown).
Based on these results, one last mouse was injected with 55 mg_{Fe} of NC34. A ΔT of 8 ^oC was accomplished within the first 29 min (see Table 3 and Figure 7b). Thermal images were acquired with infrared (IR) camera immediately after field irradiation, an example is shown in Figure 7d for a tumour injected with 200 µl of NC34 suspension (55 mg_{Fe}). IR camera image the whole tumour surface detecting IR waves from a penetration depth of about 3 mm[56]. A full agreement between fiber optic and IR camera measurements were obtained for all the tumours. These experiments show that 2.5 mg_{Fe} of NC34 dispersed in agarose (700 µL of NC34 at 3.6 mg_{Fe} mL^{-1}) induced a temperature increase of 10 ^oC but 10 mg_{Fe} of the same magnetic material induce no detectable temperature elevation in a tumour tissue (inset Figure 7d). Even more, SAR value of NC20 aqueous suspension, see table 2, is around half of that of NC34 aqueous suspension, however near the same temperature increase is obtained in tumour tissue when injected with 55 mg_{Fe}, indicating that there is no clear correlation between fluid and gel SAR and ΔT values determined in a heterogeneous tumour tissue. It is worth mentioning that we have measured the heat capacity of both materials, being 4.3±0.1 J g^{-1}°C^{-1} for 1% agarose gel and 4.2±0.1 J g^{-1} °C^{-1} for tumour tissue.

Table 3: *Ex vivo* assays results. m_{Fe} is the mass of Fe contained in the volume of NCs injected in each tumour, $[X]_{in}$ is the injected concentration, V_{tum} is the volume of each extracted tumour exposed to the AMF, Δt is the time required to reach the highest tumour temperature, ΔT represents the maximal increase of temperature with respect to a non-injected NCs tumour (control).

NC	Mouse	m_{Fe} (mg)	$[X]_{in}$ (mg mL^{-1})	V_{tum} (mm^3)	Δt (min)	ΔT (^oC)
NC20 PBS	1	55	275	150	27	5.5
	2	55	275	250	22	7.2
	3	55	275	250	23	8.5
	4	55	275	211	21	8.2
	mean value	55	275	215±47	23±3	7.4±1.4
NC34 PBS	1-2	3	32	245-384	-	-
	3	6	32	384	-	-
	4-7	10	32	320-352	-	-
	8	55	275	419	29	8
NC20 Agarose gel		51.8		700	22	16
NC34 Agarose gel		2.5		700	22	10

Next, to be certain that the NCs are still in the tumours and to compare with other authors results, the tumours were measured at a high field of 265 kHz and 40 kA m^{-1} (H_0f = *106* x 10^8 A m^{-1} s^{-1}). Heating curves of the tumours injected with PBS suspension of NC34 are shown in Figure 7c. At this high field, the heating was too fast and the higher the mass of NCs injected the faster the heating. For instance, a tumour injected with 55 mg_{Fe} of NC34 increase 22.4 ^oC in 20 s while 55 mg_{Fe} of NC20 increase 18.4 ^oC in 20 s (not shown). Other authors results[35] indicated a temperature increase of about 20 ^oC within the first 60 s in a tumour, grown with MDAMB-231 cells, loaded with 7 mg of multicore nanoparticle (composed of randomly oriented MNPs) when exposed to a high AMF of 400 kHz 25 kA m^{-1} (H_0f=*100* x 10^8 A m^{-1} s^{-1}). Our experiments have shown that tumours injected with 10 mg_{Fe} of NC34 increased 10 ^oC in 60 s at high field, indicating that our NCs pairs in quality other already characterized at high field.
An excised tumour of those grown from B16-F0 cells is shown in Figure 8. The tumour structurally consists of connective extracellular matrix, blood vessels and malignant cells, displaying thus large heterogeneities. When the NC suspension is intratumorally injected *in vivo*, the living tissue drives the NC distribution that results in an irregular NC distribution, where the NCs can end up in the interstitial extracellular matrix and in organelles such as endosomes, mitochondria and melanosomes.

Figure 8: Typical excised tumour.

Figure 9, shows TEM images of control tumours in row a) and injected with 55 mg_{Fe} of NC20 in row (b), both after AMF applications. In row a) the preservation of cellular and intracellular structures is observed. In Row b) fragmented nuclei and NCs dispersed in the cytosol and also in melanosomes are observed.

View Article Online
DOI: 10.1039/C8NR07453D

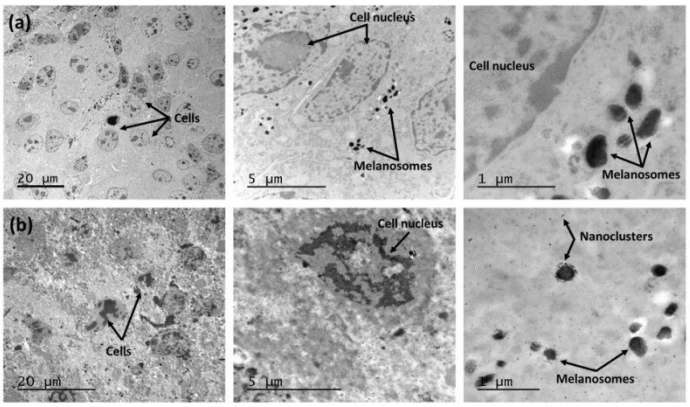

Figure 9: TEM images of B16-F0 cell tumours. Row (a) control tumour and row (b) tumour 24 h after injection with 55 mg_{Fe} of NC20 and *ex vivo* AMF of 9.3 kA m^{-1} and 100 kHz application.

Ex vivo evaluation of tumour hyperthermia left aside suppression of nanostructure effective heating due to perfusion and local thermoregulation, as well as positive adjuvant effects as cell killing and tumour regression due to possible immune response induction[57] and negative ones like the thermo-resistance phenomenon due to the induction of heat shock proteins (HSP) expression[58]. Our experiment only sense the *ex vivo* heating arising from the NCs distributed in tumour tissue as result from its interaction with living tissue. Results indicate a suppression of magnetic material effective heating efficiency which is not due to a change in viscosity and Brown mechanism inhibitions nor to aggregation phenomena inside endosomes as proposed in cell cultures[20,29,59]. As it was previously demonstrated in cancer cell cultures[23,24,26,27] we hypothesized that the irregular distribution of NC inside an heterogeneous tumour generates hot spots that are responsible for a local heating but no for a global temperature increase.

To understand whether or not this affects the therapeutic outcome further experiments are needed. It is worth mentioning that it was recently shown that cell death induced *in vivo* on colon tumours after application of MH treatment occurred without a significant global temperature increase[60].

Conclusions

We have *ex vivo* tested in tumour tissue the heating efficiency of nanoclusters composed of iron oxide magnetite nanoparticles crystallographically aligned. We found in tumour tissue a suppression of magnetic material effective heating efficiency and show that this inhibition is not due to Brown mechanism inhibition nor to NCs aggregation, instead it is related to the irregular magnetic material distribution inside the tumour. In fact, dosage had to be much increased over the values predicted from aqueous ferrofluid or agarose-gel-phantoms SAR data to achieve the same temperature increment.

We have shown that a SAR value of about 1 kW g^{-1} could not be accomplished at therapeutic field conditions in an *ex vivo* real tumour but very fast and large temperature increase was measured using high fields far off the recommended values. A word of caution should be given to studies reporting hyperthermia experiments not using therapeutically field conditions or unreal experimental settings because at these conditions non-specific heating appears due to Eddy currents. We stress the need of further integrated studies on magnetic nanostructure and tumour environment interactions that may give insight for cancer therapy.

Experimental Section

A. Chemical synthesis.

All chemical reagents used were high grade and were used without further purification. Iron(II) chloride tetra hydrate ($FeCl_2{\cdot}4H_2O$, 99%), Iron(III) chloride hexahydrate ($FeCl_3{\cdot}6H_2O$, 99%), diethylene glycol (DEG, 99%), N-methyldiethanolamine (NMDEA, 99%) were purchased from Sigma-Aldrich and sodium hydroxide (NaOH, 99.99%), sodium citrate tribasic dihydrate (98%), and nitric acid (HNO_3, 70%) from Biopak and Ultrapure agarose from Invitrogen.

Nanoclusters composed of various Fe_3O_4 nanoparticles (core) were prepared using Fe(II) and Fe(III) precursors in polyol mixture (DEG/NMDEA) via a method adapted from Hugounenq et al. In a typical procedure 1.082 g (4 mmol) of $FeCl_3{\cdot}6H_2O$ and 0.398 g (2 mmol) of $FeCl_2{\cdot}4H_2O$ were completely dissolved in 80 g of a liquid mixture of DEG and NMDEA with 1:1 (v/v) ratio at an initial temperature T_i. The solution was stirred for 1 h. Separately, a mixture of 0.64 g (16 mmol) of NaOH with 40 g of polyols was prepared. This solution was added to the solution of iron chlorides, and the resulting mixture was stirred for 3 more hours. Then, the temperature was raised to 220 °C at a heating rate of ~3 °C min^{-1}, and the mixture kept at this temperature under N_2 reflux and magnetic stirring for 12-13 h. Then, the heating mantle was switched off and the mixture slowly cooled to room temperature. The black sediments were magnetically separated and washed with a mixture of ethanol and ethyl acetate (1:1, v/v) several times to eliminate organic and inorganic impurities. Citrate anions were grafted to the surfaces of the so -produced nanoclusters by adding 0.3 mol of sodium citrate per 1 mol of iron element and kept at 60°C for 90 min. In order to eliminate citrate anions excess, the black precipitate was magnetically separated by means of a permanent magnet and centrifuged at 8000 rpm for 5 minutes, the supernatant was separated and black sediments were re-dispersed in distilled water. T_i was varied from 15 to 30 °C.

Chemical volumetric analysis, with $K_2Cr_2O_7$ used as titrant, was used for colloid concentration [x] determination[43], expressed as Fe mass per solvent volume with an accuracy of 2 %. [x] values were used to calculate SAR values from the heating curves obtained with calorimetric experiments, to normalize magnetic measurements and used as starting point to estimate the optimal Fe concentration to be injected in tumour tissue.

Agarose gels were prepared by adding 7 mg of agarose in 700 μL of aqueous suspension. The temperature of the mixture was increased up to boiling point and finally was cold down to room temperature.

B. Structural and physicochemical properties.

TEM measurements were carried out with several microscopes: 120 kV JEM-1400, 120 kV JEOL 1210, 200 kV JEM 2011,200 kV JEM JEOL 2100F, 200 kV JEM-2011 and TEM TALOS F200X. To this end, a drop of colloid was dried on carbon coated copper grids. The mean diameter and polydispersity of each system were determined by counting and

View Article Online
DOI: 10.1039/C8NR07453D
ARTICLE
Journal Name

sizing over 300 particles from TEM images using ImageJ software and fitting a Gaussian distribution to the resulting particle size histograms.
Samples for cryo-transmission electron microscopy (Cryo-TEM) were prepared as follows: 3 µL of NC suspension were placed onto a Quantifoil® grid where a perforated foil was used to bear an ultra-thin carbon support foil to minimize the total specimen thickness. The drop was blotted with filter paper and the grid was quenched rapidly into liquid ethane to produce vitreous ice, avoiding the formation of crystals. The grid was then transferred into the TEM microscope, where the temperature was kept under -140 ºC by the use of liquid nitrogen during the imaging.
Hydrodynamic diameter (D_H) was retrieved from Dynamical Light Scattering (DLS). Colloidal system stability is analysed from Z-potential (ζ) values obtained from Laser Doppler Electrophoresis measurements. A Malvern Zeta Sizer Nano ZS device equipped with a He/Ne 633 nm laser was employed. Dispersions of magnetic NCs in Milli Q water were prepared to a dilution of 1/60 of the nominal concentration; pH=7.0 to measure ζ. The same dispersions were ultrasonicated to measure the average Hydrodynamic sizes (nm). Care was taken that the DLS peak position and width were the same after three consecutive runs of 15 scans each run for all the nanoparticles. Number distribution data is reported.

C. Static magnetic measurements.

Magnetization as a function of applied magnetic field (*H*) at room temperature was obtained using vibrating sample magnetometer (VSM) Lake Shore 7404 operated with maximum applied fields $\mu_0 H_{max}$= 1.8 T and/or using a superconducting quantum interference device (SQUID) magnetometer choosing $\mu_0 Hmax$ = 2.0 T. The later was also used to achieve hysteretic magnetization loops at various temperatures between 5 and 36 K and *M vs. T* dependence under zero field cool (ZFC) and field cool (FC) protocols with H_{DC}= 4 kA m^{-1}. Magnetic measurements were performed on liquid or frozen colloids depending on the measurement temperature. A 50 µL colloidal suspension were sealed in a heat shrinkable tube to prevent sample evaporation and spills.

D. Magneto calorimetric measurements.

To determine SAR, NCs suspension (500 µL) were hold in a clear glass Dewar, agarose gel dispersion in an Eppendorf and tumours in similar plastic holder. All the experiments were carried out in non-adiabatic condition in the portable applicator is described in Section B.
Water refrigerated field generator was used for high field experiment. It consist of a resonant RLC circuit Hüttinger (2.5/300) with a water refrigerated 6 turns coil of 2.5 cm diameter with the capability of working at different frequencies up to 265 kHz and maximum field of 40 kA m^{-1}, changing capacitors and inductances.
For AMF application the samples were centred in the coil. The temperature was sensed during the whole experiment with an optical fiber sensor placed in the centre of the sample. The sensor was connected to a calibrated signal conditioner (Neoptix) with an accuracy of ± 0.1 °C. IR thermal imager Testo 870-1, of thermal sensitivity < 0.1 ºC at 30 ºC, was also used for *ex vivo* essays. The tumours were quickly removed from the coil and thermal images were obtained immediately after field irradiation. The slope *dT/dt* of the linear part of the heating curves enable to deduce the specific absorption rates (SAR)

$$\mathrm{SAR} = \frac{\mathrm{C}\ \mathrm{dT}}{[\mathrm{x}]\ \mathrm{dt}}$$

C is the volumetric heat capacity and $[\mathrm{x}]$ the concentration. Tumour tissue and agarose heat capacity was measured using modulated-differential scanning calorimetry.

E. Monte Carlo simulation.

To analyse magnetic moments alignment in the NCs , Monte Carlo simulation was carried out using the Stoner-Wohlfarth model[44] including magnetic dipolar interactions and thermal fluctuations[61] in absence of external magnetic field. The sample consist on a set of 10 NCs formed by 14 spherical monodisperse (D_{NP} = 8 nm) single domain nanoparticles crystallographically aligned. The compactness condition and excluded volume were secured. Each particle was characterized by a magnetic moment $\vec{\mu}_i$ and uniaxial anisotropy $\vec{K} = K.\hat{k}$ directed along z axis. The distances between NCs were set to be large enough in ordet to disregard the NCs interactions with respect to the intracluster particle ones. The system time evolution was carried out using the Metropolis algorithm[62,63] from a random initial magnetic moments configuration up to reach the thermal equilibrium, with open boundary conditions and the solid angle restriction proposed by Nowak[63]. The time unit, i.e. a Monte Carlo step, was defined a N attempts to update the magnetic moment of a randomly chosen particle, with N the total number of the particles in the system[64]. The results were averaged over 1000 realizations.

F. *In vitro* assays, animal model and *ex vivo* heating experiments.

Cell line and culture conditions, viability and uptake.

B16-F0 (murine melanoma, ATCC CRL-6322) were grown in RPMI-1640 (Gibco BRL, Gaithersburg, MD, USA) supplemented with 10% fetal bovine serum (FBS), 2 mM L-glutamine, 50 U mL^{-1} penicillin and 50 mg mL^{-1} streptomycin.
The cytotoxicity assay[46] of the NCs was performed with a MTT (3-[4,5-dimethylthiazol-2-yl]-2,5 diphenyl tetrazolium bromide) on B16-F0 cell line.
The cells were seeded in a 96-well plate at density of 1×10^5 cells per well in 100 µL of RPMI medium supplemented with 10% of fetal bovine serum(FBS) and incubated at 37 °C in a humidified 5% CO_2 incubator. When cells reach 90% of confluence, the medium was removed and replace by medium doped with 116 μg_{Fe} mL^{-1} concentration of NCs and incubated for 17 hours. Culture protocol was chosen with the criteria of avoiding cell culture to reach dead phase. After 17 h of incubation, the wells were washed with sterile warm PBS to remove all NC residues and replaced with 100 µL of fresh RPMI 10% FBS containing 10 µL of MTT.
After incubation time, the medium was removed and 100 µL of 0.04 N HCl in isopropanol was added to all wells and mixed to dissolve the formed violet crystals. After 30 minutes of incubation, cell viability was determined by measuring absorption at 595 nm in Amersham Bio-

View Article Online
DOI: 10.1039/C8NR07453D

Sciences Biotrak II plate reader. Results represent mean ± S.E.M. of three independent experiments.

For magnetometry of the cell cultures, a protocol previously described by Mazuel et al[65] with modifications was followed. Briefly; B16-F0 cells were cultured and incubated with NC in a 25 cm^2 flask. After incubation, medium was removed, and cell monolayer was washed three times with warm 1x PBS. Cells were detached from the flask and centrifuged at 300 xg for 5 minutes. Cell pellet was resuspended with 1x PBS and cells number (N_{cell}) were counted in Neubauer chamber. After that, cells were fixed for 15 minutes at room temperature with 4% paraformaldehyde and then washed again three times with 1x PBS. The fixed cells (more than $1x10^6$ cells to satisfy VSM sensitivity) were sealed in capsules and magnetization vs. applied field curves were obtained at 300 K by using vibrating sample magnetometer (VSM) Lake Shore 7404 operated with maximum applied fields μ0Hmax= 1.8 T to obtain the magnetic moment at saturation (μ_c) of the cell culture. Then, uptake was obtained as:

$$up - take = \frac{\mu_c}{N_{cell} M_s}$$

Where *Ms* is the saturation magnetization of the internalized NCs.

***Ex vivo* studies.**

All experiments were carried out in accordance with the National Institute of Health (NIH) Guide for the Care and the Use of Laboratory Animals, and approved by the institutional animal care and use committee (CICUAL) of the School of Pharmacy and Biochemistry, University of Buenos Aires. Female C57BL/6J mice were housed under controlled conditions and were routinely used at 8-10 weeks old (approximate weight: 20-25 g). Food and water were administered ad libitum. In order to determine the increase of temperature induced by nanocluster suspension administration, $1x10^5$ of B16-F0 cells diluted in 100 µL of RPMI were injected subcutaneously in the right flank of each mouse. 10-12 days after cell inoculation, tumour volume ~ 100 mm^3, a group of mice received two or more intratumoural injections of 100 µL of NC suspended in PBS at concentrations adjusted to achieve the desire amount of Fe. Control mice group received a PBS injection. After 24 h, mice were anesthetized via i.p. with 80 mg ketamine and 10 mg xylazine per kg of body weight, and tumours were excised and submitted to an alternate magnetic field. Temperature register was performed as described in Experimental section D. Tumour sizes were measured with a callipers and tumour volumes were calculated using the formula: $V= (D \times d^2) / 2$, where *D* is the larger diameter and *d* is the smaller.

For Transmission Electron Microscopy analysis tumours were cut into 1 mm^3 pieces after excision and fixed with 2% glutaraldehyde for two h and wash with phosphate buffer, post-fixed with 1% osmium tetroxide for 2 h at 4 °C. Then, samples were gradually dehydrated in ethanol and finally acetone, and embedded in epoxy resin for 36 h at 35, 45 y 60 °C for polymerization. Thin sections (70 nm) were cut using an ultramicrotome. The examination was performed with a JEM-1400 (JEOL USA, Pleasanton, CA, USA) transmission electron microscope equipped with an ES1000W Erlangshen charge-coupled device camera (Model No. 785; Gatan, Pleasanton, CA).

View Article Online
DOI: 10.1039/C8NR07453D

Journal Name

ARTICLE

Acknowledgements

This research was funded by CONICET (PIPs 897, 154, 524 and 567), UNLP X11/680 and X11/7884, and UBACYT 20020130100024 grants of Argentina and also partially funded by the Spanish Ministry of Economy (MAT2015-64442-R and SEV-2015-0496 projects, co-funded with European Social Funds). We acknowledge, O. Moscoso-Londoño for SQUID data acquisition and M. Knobel for the use of Instituto de Física 'Gleb Wataghin', Universidade Estadual de Campinas (UNICAMP) magnetometry instrumentation, R. Peralta for her extreme care with cell biological sample preparation for TEM, the Brazilian Nanotechnology National Laboratory (LNNano) for the use of cryo-TEM (project: ME-22346) facilities, Y-TEC S.A. for the use of TEM TALOS F200X under the supervision of A. Floridia and A. Caneiro and F.H. Sánchez, G. Pasquevich and P. Mendoza Zélis for useful discussions during field inductor building. Monte Carlo simulation were performed in UnCaFiyQT-INIFTA-SNCAD. M.B.F.v.Raap, P. C. S. Avruj, L. Rogin, A. Veiga, E. Spinelli, V.Blank, G.P. Saracco and M.A Bab are members of CONICET, and P.A. Soto is a fellow of CONICET, Argentina.

Notes and references

1 A. Jordan, R. Scholz, K. Maier-Hauff, M. Johannsen, P. Wust, J. Nadobny, H. Schirra, H. Schmidt, S. Deger, S. Loening, W. Lanksch and R. Felix, *J. Magn. Magn. Mater.*, 2001, **225**, 118–126.

2 R. E. Rosensweig, *J. Magn. Magn. Mater.*, 2002, **252**, 370–374.

3 W. S. Chang, *Cancer Res.*, 1984, **44**, 4721S–4730S.

4 A. Jordan, R. Scholz, P. Wust, H. Fähling and Roland Felix, *J. Magn. Magn. Mater.*, 1999, **201**, 413–419.

5 K. Maier-Hauff, F. Ulrich, D. Nestler, H. Niehoff, P. Wust, B. Thiesen, H. Orawa, V. Budach and A. Jordan, *J. Neurooncol.*, 2011, **103**, 317–324.

6 S. Luo, L. F. Wang, W. J. Ding, H. Wang, J. M. Zhou, H. K. Jin, S. F. Su and Ouynagm W.W., *OA Cancer*, 2014, **2**, 2.

7 M. Mahmoudi, H. Hofmann, B. Rothen-Rutishauser and A. Petri-Fink, *Chem. Rev.*, 2012, **112**, 2323–2338.

8 I. A. Brezovich, in *Medical Physics Monograph No 16: Biological, physical, and clinical aspects of hyperthermia:*, eds. B. Paliwal, F. W. Hetzel and M. W. Dewhirst, American Association of Physicists in Medicine by the American Institute of Physics, 1988, pp. 82–110.

9 W. J. Atkinson, I. A. Brezovich and D. P. Chakraborty, *IEEE Trans. Biomed. Eng.*, 1984, **BME-31**, 70–75.

10 R. Hergt, S. Dutz, R. Müller and M. Zeisberger, *J. Phys. Condens. Matter*, 2006, **18**, S2919–S2934.

11 M. Johannsen, U. Gneveckow, L. Eckelt, A. Feussner, N. WaldÖFner, R. Scholz, S. Deger, P. Wust, S. A. Loening and A. Jordan, *Int. J. Hyperth.*, 2005, **21**, 637–647.

12 U. Gneveckow, A. Jordan, R. Scholz, V. Brüß, N. Waldöfner, J. Ricke, A. Feussner, B. Hildebrandt, B. Rau and P. Wust, *Med. Phys.*, 2004, **31**, 1444–1451.

13 L. Gu, R. H. Fang, M. J. Sailor and J.-H. Park, *ACS Nano*, 2012, **6**, 4947–4954.

14 M. Marciello, V. Connord, S. Veintemillas-Verdaguer, M. A. Vergés, J. Carrey, M. Respaud, C. J. Serna and M. P. Morales, *J. Mater. Chem. B*, 2013, **1**, 5995.

15 P. Guardia, R. Di Corato, L. Lartigue, C. Wilhelm, A. Espinosa, M. Garcia-Hernandez, F. Gazeau, L. Manna and T. Pellegrino, *ACS Nano*, 2012, **6**, 3080–3091.

16 C. Martinez-Boubeta, K. Simeonidis, A. Makridis, M. Angelakeris, O. Iglesias, P. Guardia, A. Cabot, L. Yedra, S. Estradé, F. Peiró, Z. Saghi, P. A. Midgley, I. Conde-Leborán, D. Serantes and D. Baldomir, *Sci. Rep.*, 2013, **3**, 1652.

17 L. Lartigue, P. Hugounenq, D. Alloyeau, S. P. Clarke, M. Lévy, J.-C. Bacri, R. Bazzi, D. F. Brougham, C. Wilhelm and F. Gazeau, *ACS Nano*, 2012, **6**, 10935–10949.

18 P. Hugounenq, M. Levy, D. Alloyeau, L. Lartigue, E. Dubois, V. Cabuil, C. Ricolleau, S. Roux, C. Wilhelm, F. Gazeau and R. Bazzi, *J. Phys. Chem. C*, 2012, **116**, 15702–15712.

19 P. M. Zélis, G. A. Pasquevich, S. J. Stewart, M. B. Fernández van Raap, J. Aphesteguy, I. J. Bruvera, C. Laborde, B. Pianciola, S. Jacobo and F. H. Sánchez, *J. Phys. D. Appl. Phys.*, 2013, **46**, 125006.

20 J.-P. Fortin, F. Gazeau and C. Wilhelm, *Eur. Biophys. J.*, 2008, **37**, 223–228.

21 A. Makridis, K. Topouridou, M. Tziomaki, D. Sakellari, K. Simeonidis, M. Angelakeris, M. P. Yavropoulou, J. G. Yovos and O. Kalogirou, *J. Mater. Chem. B*, 2014, **2**, 8390–8398.

22 J.-H. Lee, J. Jang, J. Choi, S. H. Moon, S. Noh, J. Kim, J.-G. Kim, I.-S. Kim, K. I. Park and J. Cheon, *Nat. Nanotechnol.*, 2011, **6**, 418–422.

23 M. Creixell, A. C. Bohórquez, M. Torres-Lugo and C. Rinaldi, *ACS Nano*, 2011, **5**, 7124–7129.

24 M. E. de Sousa, A. Carrea, P. Mendoza Zélis, D. Muraca, O.

View Article Online
DOI: 10.1039/C8NR07453D

Mykhaylyk, Y. E. Sosa, R. G. Goya, F. H. Sánchez, R. A. Dewey and M. B. Fernández van Raap, *J. Phys. Chem. C*, 2016, **120**, 7339–7348.

25 C. Munoz-Menendez, I. Conde-Leboran, D. Serantes, R. Chantrell, O. Chubykalo-Fesenko and D. Baldomir, *Soft Matter*, 2016, **12**, 8815–8818.

26 M. Domenech, I. Marrero-Berrios, M. Torres-Lugo and C. Rinaldi, *ACS Nano*, 2013, **7**, 5091–5101.

27 A. Villanueva, P. de la Presa, J. M. Alonso, T. Rueda, A. Martínez, P. Crespo, M. P. Morales, M. A. Gonzalez-Fernandez, J. Valdés and G. Rivero, *J. Phys. Chem. C*, 2010, **114**, 1976–1981.

28 I. Marcos-Campos, L. Asín, T. E. Torres, C. Marquina, A. Tres, M. R. Ibarra and G. F. Goya, *Nanotechnology*, 2011, **22**, 205101.

29 S. Jeon, K. R. Hurley, J. C. Bischof, C. L. Haynes and C. J. Hogan, *Nanoscale*, 2016, **8**, 16053–16064.

30 M. Levy, C. Wilhelm, N. Luciani, V. Deveaux, F. Gendron, A. Luciani, M. Devaud and F. Gazeau, *Nanoscale*, 2011, **3**, 4402.

31 B. Kozissnik, A. C. Bohorquez, J. Dobson and C. Rinaldi, *Int. J. Hyperth.*, 2013, **29**, 706–714.

32 I. Hilger and W. A. Kaiser, *Nanomedicine*, 2012, **7**, 1443–1459.

33 I. Hilger, *Int. J. Hyperth.*, 2013, **29**, 828–834.

34 K. Mahmoudi, A. Bouras, D. Bozec, R. Ivkov and C. Hadjipanayis, *Int. J. Hyperth.*, 2018, 1–13.

35 S. Dutz, M. Kettering, I. Hilger, R. Müller and M. Zeisberger, *Nanotechnology*, 2011, **22**, 265102.

36 J. Ge, Y. Hu, M. Biasini, W. P. Beyermann and Y. Yin, *Angew. Chemie Int. Ed.*, 2007, **46**, 4342–4345.

37 J. Liu, Z. Sun, Y. Deng, Y. Zou, C. Li, X. Guo, L. Xiong, Y. Gao, F. Li and D. Zhao, *Angew. Chemie Int. Ed.*, 2009, **48**, 5875–5879.

38 L. Luo Zheng, V. Vanchinathan, R. Dalal, J. Noolandi, D. J. Waters, L. Hartmann, J. R. Cochran, C. W. Frank, C. Q. Yu and C. N. Ta, *J. Biomed. Mater. Res. Part A*, 2015, **103**, 3157–3165.

39 C. Cheng, F. Xu and H. Gu, *New J. Chem.*, 2011, **35**, 1072–1079.

40 M. B. Fernández van Raap, D. F. Coral, S. Yu, G. A. Muñoz, F. H. Sánchez and A. Roig, *Phys. Chem. Chem. Phys.*, 2017, **19**, 7176–7187.

41 D. F. Coral, P. Mendoza Zélis, M. Marciello, M. del P. Morales, A. Craievich, F. H. Sánchez and M. B. Fernández van Raap, *Langmuir*, 2016, **32**, 1201–1213.

42 R. C. O'Handley, *Modern magnetic materials : principles and applications*, Wiley, 2000.

43 M. E. de Sousa, M. B. Fernández van Raap, P. C. Rivas, P. Mendoza Zélis, P. Girardin, G. A. Pasquevich, J. L. Alessandrini, D. Muraca and F. H. Sánchez, *J. Phys. Chem. C*, 2013, **117**, 5436–5445.

44 E. C. Stoner and E. P. Wohlfarth, *Philos. Trans. R. Soc. London. Ser. A, Math. Phys. Sci.*, 1948, **240**, 599–642.

45 M. J. Benitez, O. Petracic, E. L. Salabas, F. Radu, H. Tüysüz, F. Schüth and H. Zabel, *Phys. Rev. Lett.*, 2008, **101**, 97206.

46 D. A. Wiesner and G. Dawson, *Glycoconj. J.*, 1996, **13**, 327–33.

47 A. Hanini, L. Lartigue, J. Gavard, A. Schmitt, K. Kacem, C. Wilhelm, F. Gazeau, F. Chau and S. Ammar, *RSC Adv.*, 2016, **6**, 15415–15423.

48 E. Garaio, J. M. Collantes, F. Plazaola, J. A. Garcia and I. Castellanos-Rubio, *Meas. Sci. Technol.*, 2014, **25**, 115702.

49 M. E. Cano, A. Barrera, J. C. Estrada, A. Hernandez and T. Cordova, *Rev. Sci. Instrum.*, 2011, **82**, 114904.

50 M. Beković, M. Trlep, M. Jesenik, V. Goričan and A. Hamler, *J. Magn. Magn. Mater.*, 2013, **331**, 264–268.

51 S. Dürr, W. Schmidt, C. Janko, H. P. Kraemer, P. Tripal, F. Eiermann, R. Tietze, S. Lyer and C. Alexiou, *Biomed. Eng. / Biomed. Tech.*, 2013, **58 (S1)**, 1.

52 L.-M. Lacroix, J. Carrey and M. Respaud, *Rev. Sci. Instrum.*, 2008, **79**, 93909.

53 V. Connord, B. Mehdaoui, R. P. Tan, J. Carrey and M. Respaud, *Rev. Sci. Instrum.*, 2014, **85**, 93904.

54 C. C. Tai and C. C. Chen, in *PIERS 2008 Hangzhou*, 2008, pp. 610–614.

55 S. A. Gonzalez, E. M. Spinelli, A. L. Veiga, D. F. Coral, M. B. F. van Raap, P. M. Zelis, G. A. Pasquevich and F. H. Sanchez, in *2017 IEEE 8th Latin American Symposium on Circuits & Systems (LASCAS)*, IEEE, 2017, pp. 1–4.

56 S. Stolik, J. . Delgado, A. Pérez and L. Anasagasti, *J. Photochem. Photobiol. B Biol.*, 2000, **57**, 90–93.

57 M. Suzuki, M. Shinkai, H. Honda and T. Kobayashi, *Melanoma Res.*, 2003, **13**, 129–135.

58 M. N. Rylander, Y. Feng, K. Zimmermann and K. R. Diller, *Int. J. Hyperth.*, 2010, **26**, 748–764.

59 D. Cabrera, A. Lak, T. Yoshida, M. E. Materia, D. Ortega, F. Ludwig, P. Guardia, A. Sathya, T. Pellegrino and F. J. Teran, *Nanoscale*, 2017, **9**, 5094–5101.

60 S. Kobayashi, A. Ohki, M. Tanoue, Y. Inaoka and K. Murase, *Open J. Appl. Sci.*, 2017, **7**, 647–660.

61 J. García-Otero, M. Porto, J. Rivas and A. Bunde, *Phys. Rev. Lett.*, 2000, **84**, 167–170.

62 D. Serantes and D. Baldomir, *Open Surf. Sci. J.*, 2012, **4**, 71–84.

63 U. Nowak, R. W. Chantrell and E. C. Kennedy, *Phys. Rev. Lett.*, 2000, **84**, 163–166.

64 M. E. J. Newman and G. T. Barkema, *Monte Carlo Methods in Statistical Physics*, Oxford University Press, Oxford, 1999.

65 F. Mazuel, A. Espinosa, N. Luciani, M. Reffay, R. Le Borgne, L. Motte, K. Desboeufs, A. Michel, T. Pellegrino, Y. Lalatonne and C. Wilhelm, *ACS Nano*, 2016, **10**, 7627–7638.

View Article Online
DOI: 10.1039/C8NR07453D

Highlight:

Integrated approach for the translation of magnetic hyperthermia to clinical uses. Nanoclusters of crystallographically aligned particles, validation in *ex vivo* melanoma tumour tissue and portable field inductor device.

View Article Online
DOI: 10.1039/C8NR07453D

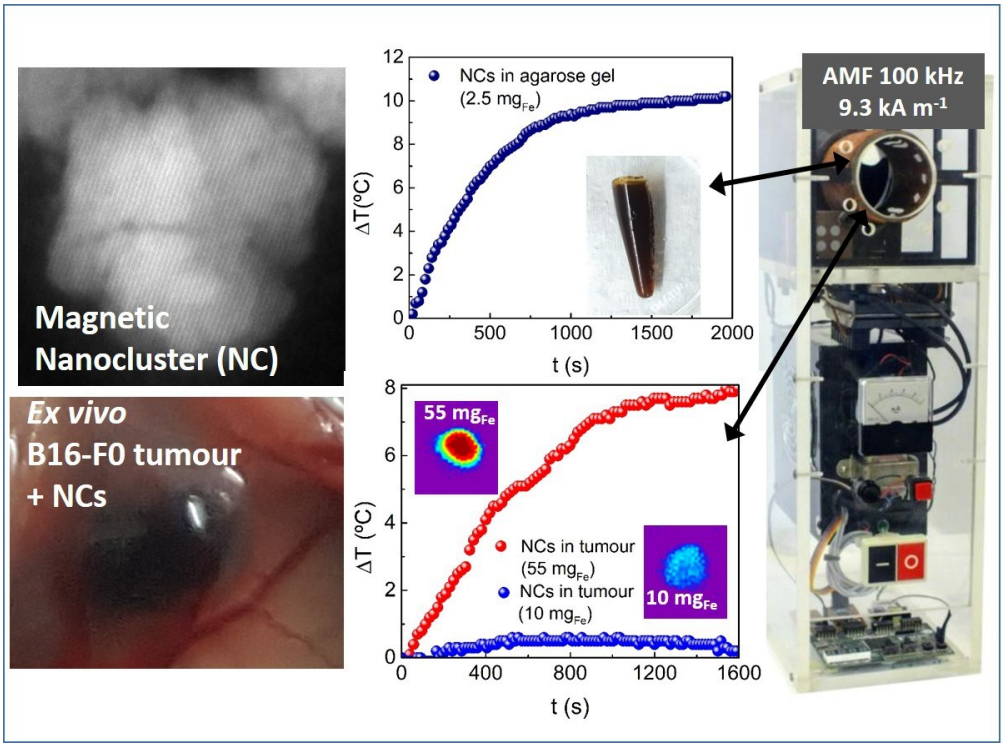

203x150mm (150 x 150 DPI)